of any other phase formation resulting from reaction between the iron and the pressure medium. Although the sample contained only MgO and iron, small traces of oxygen and water can never be totally ruled out. We watched the sample on the monitor and observed no visible reaction during heating. After the experiment, the pressure was released and the iron completely reverted to the bcc phase. None of the x-ray peaks in Fig. 2 correspond to any iron oxides (magnetite, hematite, or wustite). Although there are additional peaks that do not belong to ε (hcp) iron, the analysis is complicated by the fact that the x-ray pattern includes peaks from the untransformed hcp iron; this is because the laser beam heats only part of the iron while the x-rays pass through the entire thickness of the sample. Therefore, the dhcp peaks necessarily involve the peaks from the hcp iron as well.

The calculated lattice parameters (~38 GPa and 300 K) are a = 2.396 Å and c = 3.814 Å for the ε (hcp) phase and a = 2.427 Å and c = 7.66 Å for the dhcp phase (Fig. 3). The molar volumes for the ε and dhcp phases are 5.71 and 5.89 cm^3/mol, respectively (with unknown errors); these values are consistent with the thermodynamic assessment of such data (*4*) if the new phase is considered as β iron. Table 1 shows the calculated diffraction pattern of a sample (heated for 3.5 min) and after temperature quench (pressure maintained). Many of these peaks correspond to the ε hcp phase and not necessarily to the new phase. The calculated molar volume of the heated sample is 6.246 cm^3, as compared with 5.92 cm^3 for the quenched sample under a pressure of 35 to 40 GPa.

The x-ray study confirms that iron occurs as at least four different crystallographic structures. Because the ε (hcp) iron was the only phase recognized as a suitable high-pressure phase for Earth's core, all geophysical models of the core have been based on properties of the ε iron. We must now consider that one or more additional iron phases in Earth's core are possible.

Table 1. Calculated x-ray diffraction pattern for dhcp (a = 2.427 Å, c = 7.666 Å, Mo $K_{\alpha 1}$ radiation, P = 35 to 40 GPa, T = 300 K). I, relative intensity.

hkl	*d* (Å)	*I* (%)
100	2.1018	8
101	2.0270	45
004	1.9165	33
102	1.8429	100
103	1.6233	12
104	1.4162	5
105	1.2387	9
110	1.2135	21
106	1.0918	16
021	1.0412	4
114	1.0253	22
202	1.0135	12
023	0.9719	3
107	0.9712	3
008	0.9582	3
025	0.8668	2
206	0.8116	5

Note added in proof: Recent x-ray diffraction–laser heating measurements (*8*) also provide evidence for a new phase in a pressure-temperature range similar to that studied here.

REFERENCES AND NOTES

1. R. Boehler, *Nature* **363**, 534 (1993).
2. S. K. Saxena, G. Shen, P. Lazor, *Science* **260**, 1312 (1993).
3. O. L. Anderson, in *High-Pressure Science and Technology—1993* (AIP Conference Proceedings, American Institute of Physics, 1993), vol. 309, p. 907.
4. S. K. Saxena, G. Shen, P. Lazor, *Science* **264**, 405 (1994).
5. J. Zhang and S. K. Saxena conducted in situ heating experiments with SAM-85 equipment [from the Center for High-Pressure Research (CHiPR), State University of New York at Stony Brook] at X-17B at the Brookhaven National Laboratory during 1993 and measured the pressure and temperature transformation of bcc to fcc.
6. The sample area studied was about 35 μm by 80 μm in size. The cold pressure variation across the sample chamber was 34 to 40 GPa. The pressure measurement was based on the [200] d-spacing of MgO. The x-ray beam was 7 μm by 15 μm in size, which was similar to the size of the laser beam (diameter 15 μm). The pressure variation within the beam-size area was less than 0.5 GPa; however, there was a significant Gaussian temperature distribution over the beam-size area.
7. W. D. Pearson, *The Crystal Chemistry and Physics of Metals and Alloys* (Pergamon, New York, 1972).
8. C.-Y. Yoo *et al.*, *Science*, in press.

9. We thank J. Hu for assistance at the Brookhaven National Laboratory and colleagues at CHiPR for many useful discussions. Supported by grants from the Swedish Natural Science Research Council (NFR) and Wallenberg's Foundation.

3 May 1995; accepted 28 June 1995

Excitation of Spirals and Chiral Symmetry Breaking in Rayleigh-Bénard Convection

Robert E. Ecke,* Yuchou Hu, Ronnie Mainieri, Guenter Ahlers

Spiral-defect populations in low–Prandtl number Rayleigh-Bénard convection with slow rotation about a vertical axis were measured in carbon dioxide at high pressure. The results indicate that spirals act like "thermally excited" defects and that the winding direction of a spiral is analogous to a magnetic spin. Rotation about a vertical axis, the spiral analog of the magnetic field, breaks the zero-rotation chiral symmetry between clockwise and counterclockwise spiral defects. Many properties of spiral-defect statistics are well described by an effective statistical-mechanical model.

The discovery of spiral-defect chaos (SDC) in Rayleigh-Bénard convection (*1*) was completely unexpected and challenged long-standing theoretical ideas (*2*) about the possible states and dynamics of convection. Since the initial experimental observations, numerical simulations (*3*) and experimental work (*4*, *5*) have confirmed the robust nature of the spiral state (Fig. 1A). One aspect of spiral defects that differentiates them from defects in other systems (*6*) is that they are not constrained to be created in pairs. The spiral-defect state displays individual spirals with clockwise or counterclockwise winding (Fig. 1, B and C), targets (Fig. 1D), dipoles with the same or opposite windings (Fig. 1, E and F), and multiple-armed spirals (Fig. 1, G and H). The mechanism for the creation of such a variety of forms is unknown, but, as demonstrated by numerical simulations (*3*), a crucial element is the strength of the mean-drift field, which plays an important role in low–Prandtl number convection.

In many areas of physics an external field is helpful in probing the state of a given system. For example, a magnetic field allows for a determination of magnetization and magnetic susceptibility, which are important characteristics of systems with magnetic spins. Similarly, rotation about a vertical axis is useful in probing the SDC state. Analogies between phenomena in nonequilibrium and thermodynamic systems (for example, between bifurcations and phase transitions) and concepts from condensed-matter physics (such as orientational order) have been helpful before in the analysis of nonlinear, nonequilibrium systems (*7*). We have found that a "thermal excitation" description of spiral-defect populations works very well. Rotation about a vertical axis breaks the chiral symmetry between clockwise and counterclockwise spirals, in anal-

R. E. Ecke, Materials Science and Technology Division and Center for Nonlinear Studies, Los Alamos National Laboratory, Los Alamos, NM 87545, USA.
Y. Hu, Materials Science and Technology Division and Center for Nonlinear Studies, Los Alamos National Laboratory, Los Alamos, NM 87545, USA, and Department of Physics and Center for Nonlinear Science, University of California, Santa Barbara, CA 93106, USA.
R. Mainieri, Theoretical Division, Los Alamos National Laboratory, Los Alamos, NM 87545, USA.
G. Ahlers, Department of Physics and Center for Nonlinear Science, University of California, Santa Barbara, CA 93106, USA.

*To whom correspondence should be addressed.

ogy to the symmetry-breaking effect of a magnetic field for a paramagnet.

Statistical-mechanical spin models yield a good description of spiral populations in this nonequilibrium system despite their origins in equilibrium statistical physics. Here, we use an effective statistical-mechanical model of isolated defects to describe a complex nonequilibrium experimental system. The key to our ability to give such a description is the susceptibility of the spiral defects to rotation and our ability to probe this feature quantitatively by experiment. Numerous other nonlinear systems may be amenable to similar analysis. Our results should provide the starting point for the application of concepts from statistical mechanics to identifiable coherent structures in nonlinear systems and may indicate a deeper, as yet unestablished, theoretical foundation for these ideas.

In Rayleigh-Bénard convection, heating a thin layer of fluid from below induces convection rolls when the temperature difference ΔT exceeds a critical value ΔT_c. A reduced bifurcation parameter $\varepsilon \equiv \Delta T/\Delta T_c - 1$ describes quantitatively the degree to which the system is above the onset of convection. Another dimensionless parameter, the Prandtl number ν/κ (where ν is the kinematic viscosity and κ is the thermal diffusivity), sets the conditions for secondary instabilities in convection and is important in observations of SDC. The effect on the fluid flow of the Coriolis force arising from rotation about a vertical axis is proportional to the dimensionless rotation frequency $\Omega \equiv 2\pi f/(\nu/d^2)$, where f is the rotation frequency and d is the fluid-layer thickness. Because ΔT_c depends on Ω, we use $\Delta T_c(\Omega)$ in the expression for ε. The sign of Ω is positive when the direction of rotation is counterclockwise when viewed from above, and it is negative when the direction is clockwise when viewed from above.

Our experimental apparatus (8) consisted of a cylindrical convection cell that was enclosed in a high-pressure container and mounted on a rotating table. The cell bottom was an aluminum plate with a mirror finish and the top was an optically flat sapphire window. The circular sidewall was made of two layers of cardboard paper and had a straight vertical edge. The height of the cell was $d = 0.82 \pm 0.01$ mm. The cell radius of 42.9 mm produced a radius-to-height ratio of 52. The cell was filled with CO_2 at 32 bar (regulated to ~1 mbar) at a top-plate temperature of 33.7°C (controlled to 0.0003°C). The Prandtl number was 0.98. Convection patterns were imaged by means of the optical shadowgraph technique, which produces gray-scale images in which light and dark areas correspond to cooler and warmer fluid, respectively. Images like those in Fig. 1A were collected over the range $0.5 < \varepsilon < 1$, which corresponded to the range from the initial appearance of spirals to the constant presence of many spirals (5). The range of Ω values ($-4 < \Omega < 4$) was sufficiently small so that neither rotation-induced instabilities (9) nor large pattern distortions arising from rotation were apparent. Typically, about 120 images were recorded for each value of ε and Ω; for each image, the spirals were classified according to whether they wound toward their tips in a clockwise (c) or counterclockwise (cc) rotation (Fig. 1, B and C).

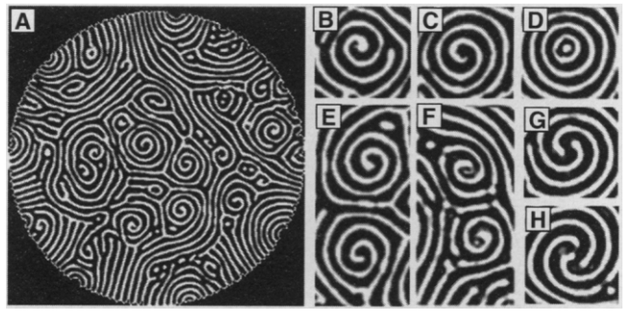

Fig. 1. Spiral defect patterns ($\varepsilon = 0.84$, $\Omega = 0$). (**A**) Full cell; (**B**) clockwise (c); (**C**) counterclockwise (cc); (**D**) target; (**E**) cc:cc dipole; (**F**) c:cc dipole; (**G**) double arm; (**H**) triple arm.

A complete description of the convection rolls in the experiment would require a continuum model. Suppose, however, that the state of the system can be described approximately by the number of c and cc spirals. Then the essential statistical quantity that characterizes this state is the probability distribution of the number of c and cc spirals as a function of ε and Ω. We used this distribution to compute all other statistical properties of the state, including the average number of spirals (a quantity that depends on the system size) and the ratio or difference between average numbers of c and cc spirals (which are independent of system size); the statistical errors of these quantities were estimated by assuming that the root-mean-square fluctuation amplitudes for a sample of size N are equal to $\sqrt{N}$. We then compared these quantities with the predictions of two statistical-mechanical models. The first is a noninteracting two-state model in which each spiral is represented by a single spin and the analytic expressions are simple. The second is a one-dimensional spin-1, nearest-neighbor interaction model in which each spiral is represented by a group of spins and the analytic expressions are complicated. Both models have the same number of free parameters, and in both the spirals do not interact. The main difference between the models is that the spin-1 model can account for the experimentally observed higher probability of spirals of smaller size. Details of the models are presented elsewhere (*10*).

The shape of the probability distribution ρ for the number of spirals m in any one image depends on the correlations between spiral-nucleation events. In Fig. 2A, we show ρ for $\varepsilon = 0.80$. For independent identical events, applicable to the two-state model, a Poisson distribution (the solid line in the plot) would be expected and was calculated with no adjustable parameters from the mean value of the data set. The dashed line was calculated from the spin-1 model with the use of parameters from fits described below but with no independent adjustment to fit the probability distribution. Within statistical uncertainty, the distributions are consistent with either model. For $\varepsilon = 0.96$ (Fig. 2B) the two models give different distributions, with the spin-1 mod-

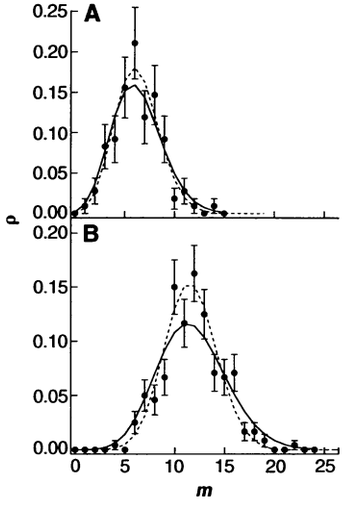

Fig. 2. Plots of ρ versus m. (**A**) $\varepsilon = 0.80$; (**B**) $\varepsilon = 0.96$. Solid lines are Poisson distributions; dashed lines are calculated from the spin-1 model.

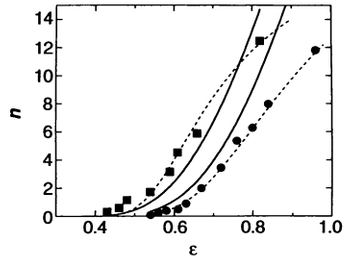

Fig. 3. Plots of n versus ε (■, $\Omega = 0$; ●, $\Omega = 4$). Solid curves are fits to the two-state model; dashed curves are fits to the spin-1 model.

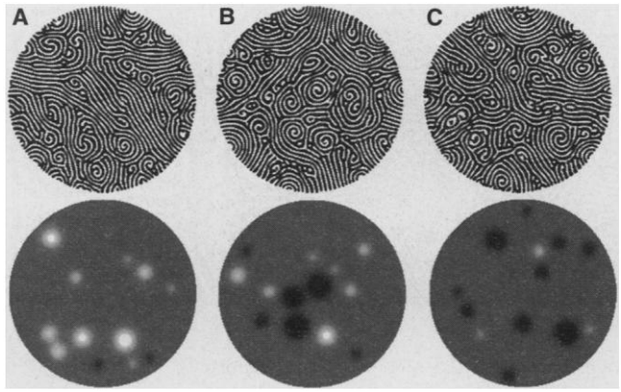

Fig. 4. Convection patterns (upper panel) and spiral locations (white, c; black, cc) (lower panel). (**A**) $\Omega = -4$, $\varepsilon = 0.74$; (**B**) $\Omega = 0$, $\varepsilon = 0.84$; (**C**) $\Omega = 4$, $\varepsilon = 0.82$.

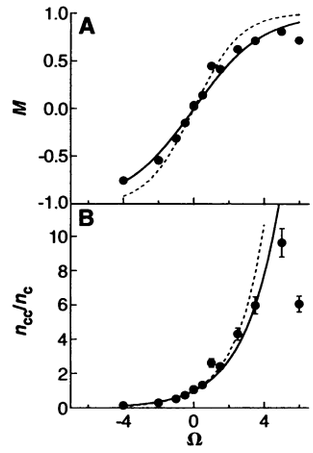

Fig. 5. (**A**) Plot of M versus Ω; (**B**) plot of n_{cc}/n_c versus Ω. Solid curves are fits to the two-state model; dashed curves are fits to the spin-1 model.

el describing the data better. The agreement between the data and the models strongly indicates noninteracting spiral nucleation, but the spin-1 model better accounts for the decreased probability of spirals of larger size.

The average number n of spirals per image is the sum of the average number of clockwise spirals n_c and counterclockwise spirals n_{cc}. Figure 3 shows n as a function of ε for $\Omega = 0$ and $\Omega = 4$. The number of spirals increased rapidly with ε, and at a particular ε it was much larger for the $\Omega = 4$ data set. The difference in n_{cc} and n_c as a function of the rotation rate is illustrated in Fig. 4, which shows representative images of patterns with negative, zero, and positive rotation ($\Omega = -4$, 0, and 4). The instantaneous number of c and cc spirals changed with time, and hence these representative images were chosen so that the ratios of the numbers of c and cc spirals were the same as the average n_{cc}/n_c values. Also shown in Fig. 4 are corresponding images of the locations of c and cc spirals. From these images it is clear that rotation had a dramatic effect on the relative populations of c and cc spirals. This effect is illustrated quantitatively in Fig. 5, which shows the ratio n_{cc}/n_c and the normalized difference $M \equiv (n_{cc} - n_c)/(n_{cc} + n_c)$ for a range of Ω values ($\varepsilon \approx 0.75$). The antisymmetric form of M with respect to Ω indicates the chiral symmetry–breaking property of the rotation (Fig. 5A). The ratio n_{cc}/n_c indicates a rapid splitting of the spiral populations as Ω increases (Fig. 5B).

These results are reproduced reasonably well by either of the two models described above. In either case we solved the statistical mechanics for a Hamiltonian of the form $\Sigma_{\{i\}} h\sigma_i + \Sigma_{\{i,j\}} E(\sigma_i,\sigma_j)$, where σ_i are the components of spin, $\{i\}$ or $\{i,j\}$ represent all possible spins, $h = a\Omega$ is the field strength, a is the scale of the rotation field, and $E(\sigma_i,\sigma_j)$ is an interaction-energy function. For the two-state model, $i = \{-1,+1\}$, $E(\sigma_i,\sigma_j) = 0$, and we used the grand-canonical ensemble with a chemical potential J to adjust the relative spin populations. For the spin-1 model, $i = \{-1,0,+1\}$, $E(\sigma_i,\sigma_j) = 0$ if $\sigma_i = \sigma_j = 0, \infty$ if $\sigma_i = -\sigma_j \neq 0$, and J otherwise, and the canonical ensemble was used. For simplicity we will discuss the analytic results for the two-state model only [the solutions for the spin-1 model were obtained by means of transfer-matrix techniques (*10*)]. The rapid rise in n, the average number of spins, as a function of ε is an exponential "Arrhenius" activation of the form $n = V \exp[-F/(\varepsilon - \varepsilon_0)]$, where V is the size of the system, F is an effective "energy" with value J for $\Omega = 0$, and ε_0 is the zero of the effective temperature scale. For n_{cc} and n_c the quantity F is modified by rotation in the same way that a magnetic field shifts the energy of magnetic spins, that is, $F = J \pm a\Omega$. The ratio is then $n_{cc}/n_c = \exp[2a\Omega/(\varepsilon - \varepsilon_0)]$, the same form as for spins. The difference M is highly reminiscent of spin magnetization, in which a sigmoid-shaped curve of the form $M = \tanh[a\Omega/(\varepsilon - \varepsilon_0)]$ is expected. For this to be the compelling description, the model must be simple with a minimum of free parameters and it must also relate the different data sets in a self-consistent manner.

Both of the models described above can be fit to the data by adjusting the four independent parameters ε_0, a, J, and V. A least-squares fit of the excitation data in Fig. 3 to the two-state model yields $\varepsilon_0 = 0.21$, $a = 0.14$, $J = 2.4$, and $V = 255$ and the solid curves in Fig. 3. Without any adjustment of parameters, it also yields the solid curves in Fig. 5. The values of n_{cc}/n_c and M agree well but the fits to the excitation data are not very good, which is surprising because the fits were to the average numbers and not to the values of n_{cc}/n_c or M. Alternatively, fitting the spin-1 model to the four data sets $n(\varepsilon,\Omega = 0)$, $n(\varepsilon,\Omega = 4)$, n_{cc}/n_c, and M produces $\varepsilon_0 = 0.34$, $a = 0.13$, $J = 0.76$, and $V = 86.5$. The dashed curves in Figs. 2, 3, and 5 show the results with these parameters. The agreement is quite good with the exception of M and n_{cc}/n_c for $|\Omega| > 2$. These deviations may indicate that the data for $|\Omega| > 2$ are already outside the region in which Ω can be considered a small perturbation. Overall the spin-1 model gives a better description of the whole system, including the probability distributions of the number of spirals at high values of ε (Fig. 2) and the distribution of spiral sizes (*10*). On the other hand, the two-state model is simple and includes many of the essential ingredients of the physical system. Apparently, the size of spirals matters, and this factor is accounted for in the spin-1 model but not in the two-state model.

The analogy between the spin system and the SDC state has been extremely useful in organizing our thinking about this state. More realistic models (for example, a two-dimensional model) might be formulated, but at the cost of further complication and more adjustable parameters in the model. Some possibly related theoretical work on statistical-mechanical formulations of nonequilibrium states has been done (*11*), but more directed theoretical efforts are needed to connect with our experiments. In any event, the response of spiral-defect populations to rotation as reflected in the asymmetry of spiral populations is an intriguing clue in the understanding of this nonlinear system.

REFERENCES AND NOTES

1. S. W. Morris, E. Bodenschatz, D. S. Cannell, G. Ahlers, *Phys. Rev. Lett.* **71**, 2026 (1993).
2. M. C. Cross and P. C. Hohenberg, *Rev. Mod. Phys.* **65**, 851 (1993).
3. H.-W. Xi, J. D. Gunton, J. Vinals, *Phys. Rev. Lett.* **71**, 2030 (1993); W. Decker, W. Pesch, A. Weber, *ibid.* **73**, 648 (1994).
4. M. Assenheimer and V. Steinberg, *Nature* **367**, 345 (1994).
5. Y. Hu, R. E. Ecke, G. Ahlers, *Phys. Rev. Lett.* **74**, 391 (1995).
6. See, for example, P. Coullet, L. Gil, J. Lega, *ibid.* **62**, 1619 (1989); I. Rehberg, S. Rasenat, V. Steinberg, *ibid.*, p. 756.
7. R. Occelli, E. Guazzelli, J. Pantaloni, *J. Phys. Lett.* **44**,

567 (1983); N. Tufillaro, R. Ramshankar, J. Gollub, *Phys. Rev. Lett.* **62**, 422 (1989).
8. Y. Hu, R. E. Ecke, G. Ahlers, *Phys. Rev. E* **48**, 4399 (1993).
9. G. Küppers and D. Lortz, *J. Fluid Mech.* **35**, 609 (1969).
10. R. E. Ecke, Y. Hu, R. Mainieri, G. Ahlers, unpublished data.
11. R. Graham and T. Tél, in *Instabilities and Nonequilibrium Structures III*, E. Tirapegue and W. Zeller, Eds. (Kluwer, Dordrecht, Netherlands, 1991), pp. 125–142.
12. We thank N. Li and M. Cross for useful discussions. Supported by the U.S. Department of Energy and a grant from the Institutional Collaborative Research Program (INCOR), University of California.

13 April 1995; accepted 27 July 1995

Laser Separation of Geometrical Isomers of Weakly Bound Molecular Complexes

Charles Desfrançois, Hassan Abdoul-Carime, C. P. Schulz, Jean Pierre Schermann*

Molecular assemblies held together by weak intermolecular bonds exhibit a rich variety of geometries. Even a simple complex formed by only two molecules can adopt several conformations corresponding to different geometrical isomers. Isomers of small polar dimers can be isolated nondestructively by taking advantage of a selective and reversible ionization process, with the use of a mass spectrometry method that allows the determination and control of the geometrical configuration of neutral or negatively charged molecular complexes in supersonic beams. Here, the method is applied to isolated nucleic acid base pairs that can be selected in stacked or H-bonded configurations.

The understanding of van der Waals or hydrogen interactions under nearly ideal conditions in the gas phase is one of the main purposes of molecular cluster experimental and theoretical studies. Such clusters are usually produced in supersonic beam expansions that yield broad mass distributions. Ionization techniques used in standard mass spectrometry to allow mass selection may strongly modify the initial neutral cluster structures. Nondestructive mass selection of neutral clusters requires sophisticated methods (*1*, *2*); it has been shown that for a given cluster mass, several isomer configurations can still coexist in a beam (*1*, *3*, *4*). The aim of our work here is to show how such isomers can be spatially separated; to achieve this, we had to find parameters that are strongly sensitive to the molecular geometry, allowing ionization processes that do not modify or destroy the selected molecular structure.

In closed-shell polar systems, electrons can be reversibly attached outside the molecular frame, thus providing such a nondestructive ionization process. At large distances r from polar molecules or clusters, excess electrons are attracted by the charge-dipole $-\mu/r^2$ potential (*5*), whereas they suffer repulsion at very short distances. Electrons can thus be trapped in a potential well if the attractive dipole moment μ is larger than 2.5 D (*6*), leading to dipole-bound anions that essentially retain the geometrical configuration of their neutral parents. For example, although single water (μ = 1.854 D) or single ammonia molecules (μ = 1.471 D) are not able to bind excess electrons, a water-ammonia complex can (*7*). The excess electron orbitals are extremely diffuse, and the corresponding electron binding energies are very weak (0.1 to 100 meV). Easily accessible external electric fields (0.1 to 30 kV cm^{-1}) are sufficient to detach the excess electrons (*8*) and therefore allow for a reversible ionizing process. These fragile anions cannot be produced by simple attachment of low-energy free electrons to cold neutral clusters because the presence of a third body is necessary to avoid the reverse process (electron autodetachment). However, dipole-bound anions can be preferentially prepared in collisions between polar systems and highly excited Rydberg atoms in which external electrons are already in very diffuse orbitals; the role of the stabilizing third body is then played by the Rydberg atom ionic core. The signature of the presence of a dipole-bound anion is the appearance of a more or less sharp peak in the anion creation rate as a function of the Rydberg atom orbital size—that is, the principal quantum number n of the Rydberg state (*9*). In contrast, a smooth dependence of the anion rate on n corresponds to the creation of a conventional anion where the excess electron enters a molecular orbital (*10*).

Polar clusters were prepared in a supersonic beam expansion; subsequently, the cluster beam crossed a beam of Rydberg atoms (Fig. 1). Electron exchange took place, and the anions were observed in a time-of-flight setup. An external electric field, created by a set of grids perpendicular to the anion beam (*6*, *8*), can detach the anion excess electron. Above a threshold electric field, which is characteristic of the electron binding energy, anions are transformed back to neutral clusters; this was easily verified by letting them pass through an additional negative repulsive grid. Our mass spectrometry technique can therefore be applied to the production of either charged or neutral geometrically selected complexes.

We can detect only the existence of complexes rather than their geometries, and therefore a comparison between model calculations and experimental measurements of resultant dipole moments is required to deduce structural information. As a first example, let us consider a dimer that results from the mixture of water and acetonitrile molecules. A first experiment (*11*) has shown the existence of a geometrical configuration with a large resultant dipole moment (5.5 D), corresponding to anions that can be produced only by charge exchange with low-lying Rydberg states. This observation was confirmed by a calculation that also

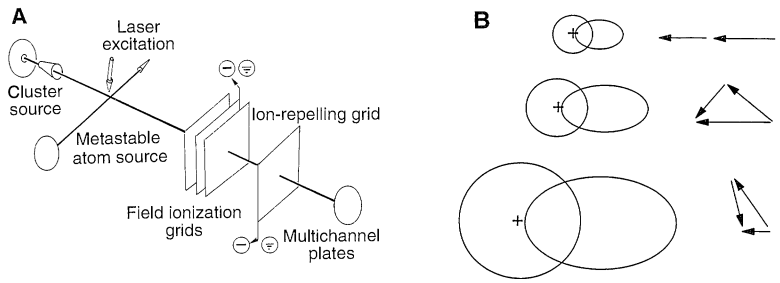

Fig. 1. (**A**) Schematic drawing of the crossed beam experiment used for mass and geometry selection of the different components of a polar cluster beam. Metastable atoms are produced by electron bombardment of xenon (Xe) atoms and are further excited toward Rydberg states by means of a tunable laser. The Rydberg atoms can transfer their external electron to polar clusters, leading to dipole-bound anions. To obtain neutral clusters, we applied an external electric field for detachment of the anion excess electrons. (**B**) Each geometrical configuration of the dipoles corresponds to a resultant dipole moment of the molecular clusters, leading to different dipole-bound anions. In these anions, excess electrons are in diffuse orbitals that are well matched for electron exchange by different Rydberg atom orbitals.

Laboratoire de Physique des Lasers, Université Paris-Nord Villetaneuse 93430, France.

*To whom correspondence should be addressed.